Combined disturbance-observer-based control and iterative learning control design for pulsed superconducting radio frequency cavities

Feng Qiu[1,2,3] · Shinichiro Michizono[1,2] · Toshihiro Matsumoto[1,2] ·
Takako Miura[1,2]

Abstract The development of iterative learning control combined with disturbance-observer-based (DOB) control for the digital low-level radio frequency (LLRF) system of the International Linear Collider project is presented. The objective of this study is to compensate for both repetitive (or predictable) and unpredictable disturbances in a radio frequency system (e.g., beam loading, Lorentz force detuning, and microphonics). The DOB control approach was verified using the LLRF system at the Superconducting Test Facility (STF) at KEK in the absence of a beam. The method comprising DOB control combined with an iterative learning control algorithm was then demonstrated in a cavity-simulator-based test bench, where a simulated beam was available. The results showed that the performance of the LLRF system was improved, as expected by this combined control approach. We plan to further generalize this approach to LLRF systems at the STF and the future International Linear Collider project.

Keywords Low-level radio frequency · Disturbance observer · Iterative learning control

✉ Feng Qiu
   qiufeng@impcas.ac.cn

1   High Energy Accelerator Research Organization, 1–1 Oho,
    Tsukuba, Ibaraki 305–0801, Japan

2   The Graduate University for Advanced Studies,
    Shonan Village, Hayama, Kanagawa 240–0193, Japan

3   Institute of Modern Physics, Chinese Academy of Sciences,
    Lanzhou 730000, China

1 Introduction

The International Linear Collider is a proposed electron and positron collider accelerator that aims to precisely investigate the Higgs boson, dark matter, and possible extra dimensions. A total of 400 radio frequency (RF) stations, each equipped with 39 superconducting (SC) RF nine-cell cavities driven by a 10-MW multi-beam klystron, were installed in the International Linear Collider [1]. The superconducting test facility (STF) was constructed at KEK to develop key technologies related to the International Linear Collider (e.g., high-gradient SC cavities, higher-order mode couplers, high-power RF sources, and high-precision RF control systems). The current status of the STF is illustrated in Fig. 1 [2–4]. The injector consists of a photocathode RF gun and two SC nine-cell cavities in a capture cryomodule. These two cavities are driven by an 800-kW klystron. The beam was accelerated to 40 MeV at the injector output. The main linac was constructed in two phases. In the first phase (current status), a total of 12 SC nine-cell cavities within two cryomodules (CM1 with eight cavities and CM2a with four cavities) driven by a 10-MW multi-beam klystron were installed; however, four cavities (#5–7 and #9) suffered from degradation caused by heavy field emission [4]. Therefore, only eight SC cavities are operated in the current state.
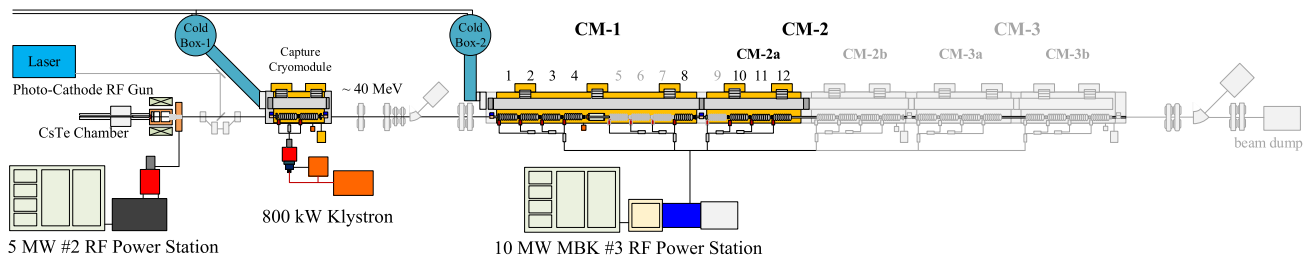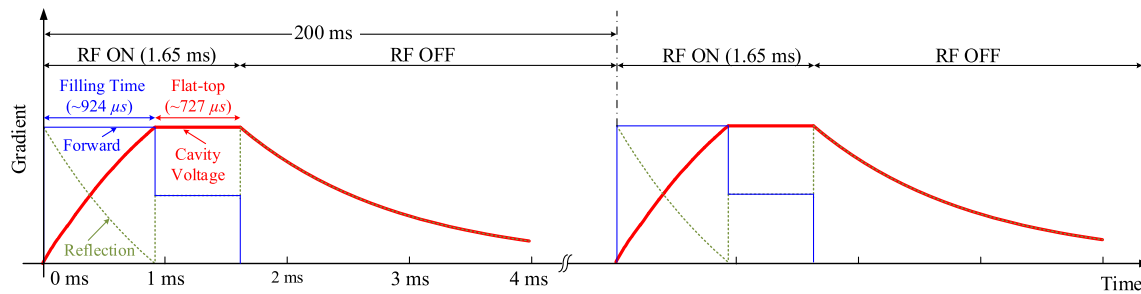
The SC cavities in the International Linear Collider and STF were operated in pulse mode with a 1.65-ms pulse duration and a 5-Hz repetition rate [1, 2]. The typical forward pulses from the klystron, reflection, and cavity signal are shown in Fig. 2. The cavity voltage was gradually increased to its design value during the filling time ($\sim 924\ \mu$s) and was then kept constant ("flat") during the flat-top time ($\sim 727 \mu$s) when beam is accelerated. To

Fig. 1 (Color online) Current status of the STF project. SC cavities #5–7 and #9 in the main linac suffer from degradation caused by heavy field emissions

Fig. 2 (Color online) Typical RF forward pulse (in blue), reflection (green dotted curve), and cavity field signal (in red) in the absence of a beam. The pulse signal consists of the filling time and flat-top time

achieve high beam quality, the RF field fluctuation during the flat-top acceleration should be maintained at <0.07% (root mean square (RMS)) for the amplitude and 0.35° (RMS) for the phase [1]. Low-level RF (LLRF) systems based on field-programmable gate arrays (FPGAs) are applied to stabilize the RF field during the flat-top acceleration.

In practice, the RF system is disturbed by various factors that can be classified into two categories: repetitive (predictable) disturbances and unpredictable disturbances [5]. Repetitive disturbances such as Lorentz force detuning (LFD) and beam loading are repeated in the system from pulse to pulse [6, 7]. Unpredictable disturbances such as microphonics are generally not synchronized with the RF operation and vary from pulse to pulse. All these disturbances limit the performance of the LLRF system. Usually, proportional and integral (PI) control and proportional (P) control are widely used in the LLRF system to remove these disturbances and errors; however, PI or P control is usually insufficient in the presence of higher frequencies and greater intensity disturbances (e.g., in case of large beam loading or the presence of the LFD effect). These issues have motivated us to search for other advanced control approaches in addition to traditional PI control. Repetitive disturbances can be removed by iterative learning control (ILC) [8–13]. ILC algorithms were originally developed for robot learning and training by Uchiyama and Arimoto [8, 9]. In this control strategy, the error information gathered from the last cycle is estimated

and used to improve the current cycle. An ILC algorithm requires the system to perform the same action repeatedly. This requirement can be fulfilled in a pulse-mode operation accelerator, such as the International Linear Collider and STF. Applications of the ILC algorithm related to the LLRF field can be found in [10, 11, 14]. However, the ILC algorithm is incapable of rejecting unpredictable disturbances such as microphonics. In view of this situation, a disturbance-observer-based (DOB) control method was introduced to suppress these errors. This approach was first introduced by Ohnishi [15] and refined by Umeno and Hori [16]. DOB control was successfully applied to the LLRF system of the compact energy recovery linac (cERL) test facility at KEK [5, 17–20], demonstrating that DOB control is effective for both repetitive and unpredictable disturbances. This has motivated us to design a control algorithm that combines the advantages of ILC and DOB, and both repetitive and unpredictable errors are expected to be canceled in the combined control approach.

This study focuses on the design and development of the combined control approaches mentioned above. Applications of the approach to the STF and a cavity-simulator-based test bench are presented. The remainder of this paper is organized as follows. Section II briefly introduces the typical LLRF system used in the accelerators. Section 3 describes the principles of the ILC algorithm and DOB control. Section 4 presents the design of the combined control approach. Section 5 presents the results of the combined P- and DOB-based (P + DOB-based)

applications at the STF, as well as the applications of the combined P-, DOB-, and ILC-based (P + DOB + ILC-based) control on a cavity-simulator-based test bench. Finally, Sect. 6 summarizes these combined control approaches.

2 LLRF system

Figure 3 illustrates the block diagram of a typical LLRF system [21, 22]. The RF pick-up signals from all cavities in the cryomodule are down-converted to intermediate frequency (IF) signals. The IF signals are sampled in the next stage and fed into an FPGA. The baseband in-phase and quadrature (I/Q) components are extracted from the digitalized IF signals by a digital I/Q detection model [23, 24]. The I/Q signals are fed into a 2×2 rotation matrix to correct the loop phase. The vector-sum signal is then obtained by calculating the superposition of all the cavity pick-up signals. After being filtered by digital filters, the I/Q components of the vector-sum signal are compared

with their set values and the I/Q errors are calculated. Then, the I/Q errors are regulated by a PI feedback (FB) controller. The processed I/Q signals are added to their corresponding feed-forward (FF) models. The combinational signals are fed into the I/Q modulator by a digital-to-analog converter to modulate the 1.3-GHz RF signal from the oscillator. Finally, the LLRF feedback loop is closed by means of a high-power source, which drives the cavities.

Typical sources of disturbances in an RF system are shown in Fig. 3. Repetitive disturbances such as LFD and beam loading are repeated from pulse to pulse. In contrast, unpredictable disturbances such as microphonics usually vary from pulse to pulse [5–7]. In a pulsed-mode accelerator, using traditional PI control is usually insufficient for removing all of these disturbances. Many advanced control algorithms such as H_∞ multi-input–multi-output control [10], DOB control [5], learning control [10, 11], and active disturbance rejection control [25] have been applied to further improve the performance of LLRF systems. The International Linear Collider and STF are operated in the pulse mode, which means that the RF system performs the same action repeatedly. The ILC algorithm is very
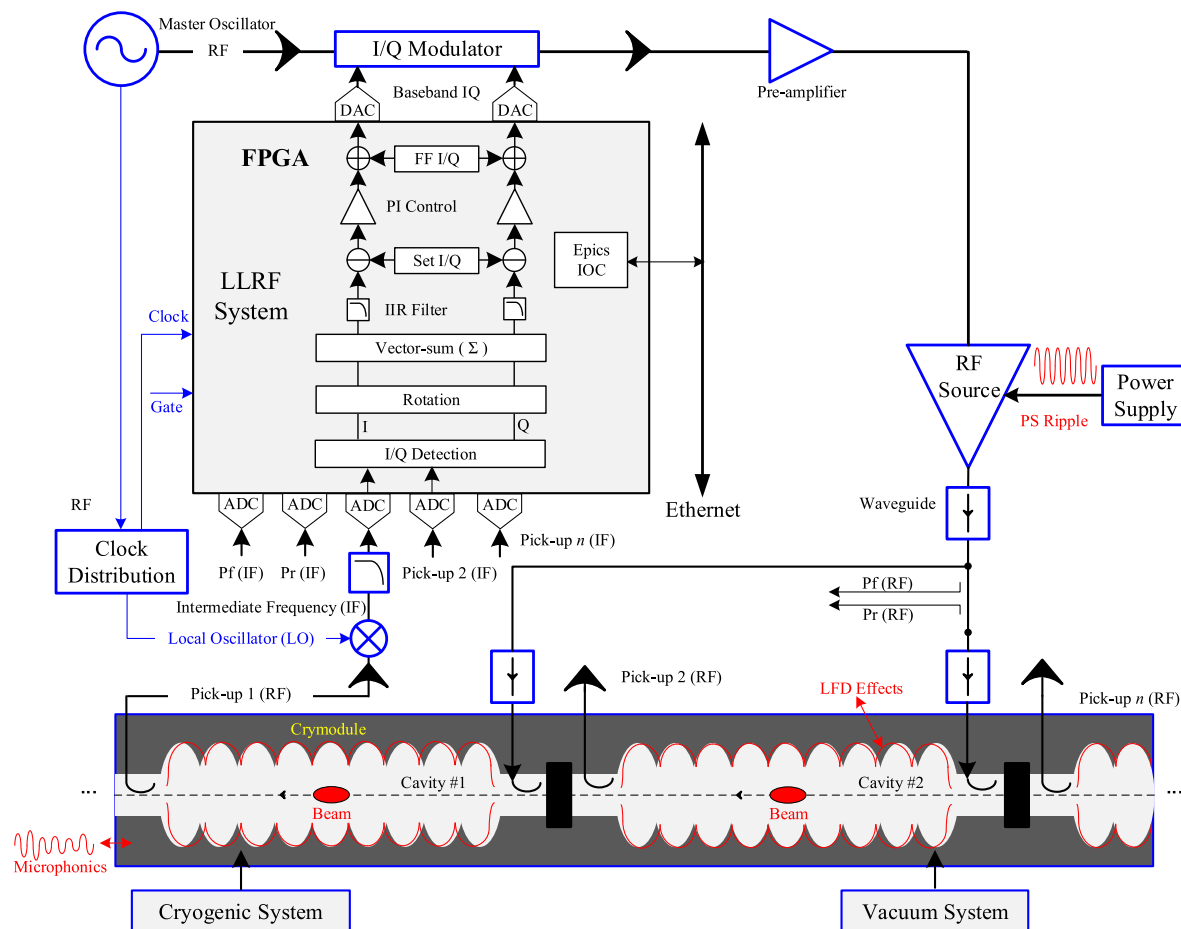
Fig. 3 (Color online) Diagram of a typical LLRF system

effective in removing repetitive disturbances in a system that has repetitions. DOB control is a good choice for managing unpredictable disturbances, such as microphonics. This control method has been successfully applied to the LLRF system of the cERL, which is a continuous wave mode facility [5, 17–19]. Although DOB control is effective for both repetitive disturbances and other unpredictable disturbances, the effective bandwidth is usually limited by the bandwidth of the Q-filter. In view of this situation, we are motivated to combine the advantages of these two control approaches to cancel all the repetitive and unpredictable disturbances. The combined method is discussed in the following section.

3 Principles of ILC and DOB control

In this section, we briefly introduce the principles of ILC and DOB control.

3.1 Principle of the ILC algorithm

Consider a discrete-time system G_p in the jth trial:

$$\begin{cases} x_j(k+1) = Ax_j(k) + Bu_j(k) \\ y_j(k) = Cx_j(k) \end{cases}, \tag{1}$$

where the matrices A, B, and C describe the discrete-time system in the state space, and $x_j(k)$, $u_j(k)$, and $y_j(k)$ are the state, control, and output variables, respectively. The subscripts "j" and "k" represent the iteration index and time index, respectively.

A widely used ILC learning algorithm is [12, 13]

$$u_{j+1}(k) = Q_{ILC}\left[u_j(k) + L(e_j(k))\right], \tag{2}$$

where Q_{ILC} and L are defined as the Q-filter and learning function, respectively.

Figure 4 illustrates the learning process of the ILC algorithm used in an LLRF system with pulse mode operation (e.g., the LLRF system at the International Linear Collider and STF). In the jth trial, the cavity error signal $e_j(k)$ is learned using the learning function L. The result $L(e_j)$ is added to the jth control signal $u_j(k)$. The combined signal was filtered using a Q-filter. The Q-filter is usually a low-pass filter employed to enhance the robustness of ILC. The output signal was then updated using the filtered signal. In the $(j+1)$th trial, the cavity signal is detected first, and then this is compared with the given reference signal r to calculate the new error signal, $e_{j+1}(k)$. This algorithm was implemented at each repetition, and the tracking accuracy was improved in this iterative process.

A block diagram of the ILC algorithm is presented in Fig. 5. In the ILC algorithm, the learning function L and Q-filter Q_{ILC} are very significant. For the learning function, the simplest L is a proportional gain P. In this case, the learning updated algorithm in Eq. (2) is simplified as

$$u_{j+1}(k) = Q_{ILC}\left[u_j(k) + Pe_j(k)\right]. \tag{3}$$

The algorithm shown in Eq. (3) is defined as a P-type ILC. In our study, we first applied a P-type ILC because of its ease of design and implementation. Many advanced ILC algorithms, such as higher order ILC, H_∞-based ILC, plant-inversion-based ILC, and optimization-based ILC, have been proposed for performance improvement, fast convergence rate, and robustness [12, 13]. A norm-optimization-based ILC was applied at DESY [10, 11]. In our study, we selected the plant-inversion-based ILC algorithm owing to its fast convergence rate. The algorithm of a plant-inversion-based ILC can be expressed as [12, 13]

$$u_{j+1}(k) = Q_{ILC}\left[u_j(k) + G_n^{-1}e_j(k)\right], \tag{4}$$

where $G_n(z)$ represents the nominal model of the actual system $G_p(z)$. The learning function is $L = G_n^{-1}(z)$. To
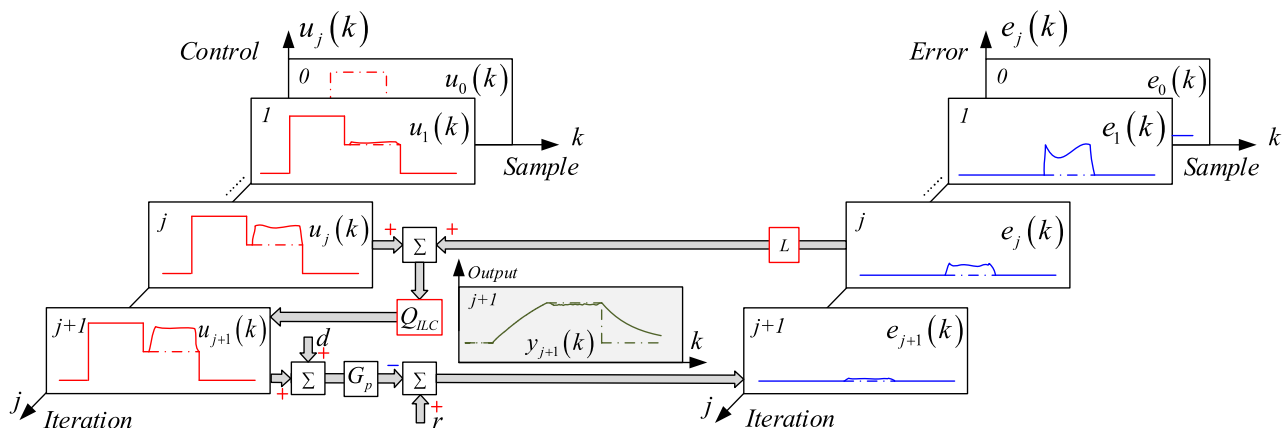
Fig. 4 (Color online) Principle of the ILC algorithm in the LLRF system
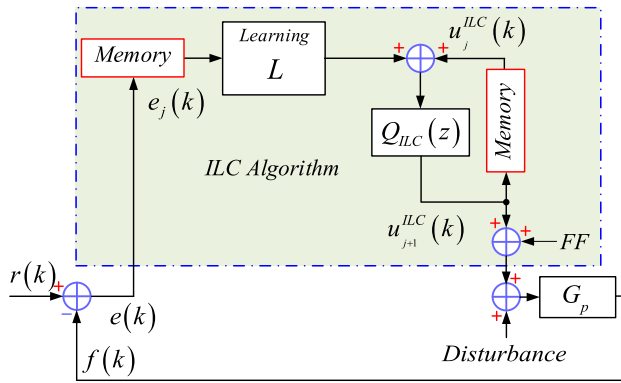
Fig. 5 (Color online) Architecture of the ILC FF algorithm in the LLRF system

avoid poor transients caused by model uncertainty, the bandwidth of the Q-filter should be set to a sufficiently low frequency [12].

It should be mentioned that the Q-filter and learning function can be noncausal. For example, we can define the Q-filter as a zero-phase low-pass filter, which is a noncausal filter that allows for high-frequency attenuation without any phase lag [12]. The transfer function of the zero-phase conventional finite impulse response (FIR) filter is given by

$$H(z) = \sum_{k=-N}^{k=N} b_k z^{-k}, \tag{5}$$

where b_k is a vector of coefficients that are symmetric about $k = 0$. For comparison, the transfer function in the case of the conventional FIR filter is

$$H(z) = \sum_{k=0}^{k=M} c_k z^{-k}, \tag{6}$$

where c_k is the coefficient of the filter. The reason for applying a zero-phase filter is to reduce the final error levels of the steady state [26]. Figure 6 compares the filtered error signals using different filters. The conventional
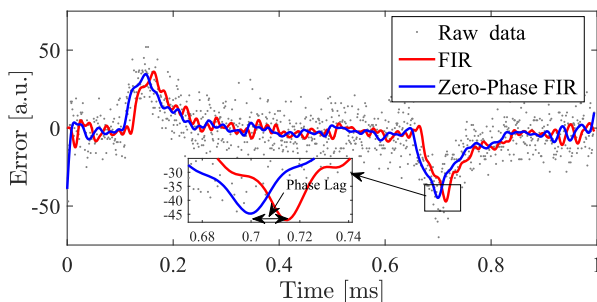
Fig. 6 (Color online) Comparison of different filters. The zero-phase FIR filter (in blue) provides better performance than the usual FIR filter (in red)

FIR filter is of the 30th order and has a 50-kHz bandwidth. The zero-phase FIR filter is of the same order and bandwidth as above. The sampling rate is ~ 1 MHz in our case. The phase difference can be observed in the output of the conventional FIR filter and the zero-phase FIR filter. The MATLAB function *filtfilt* was used to construct the zero-phase filter [27].

3.2 DOB control

DOB control was originally proposed in [15]. The key component of DOB control is a disturbance observer capable of estimating the disturbances of the system. The structure of DOB control is illustrated in Fig. 7. Signals c, ε, d, and $\hat{d}$ represent the control, plant input, disturbance, and disturbance estimate, respectively. Models G_p and G_n represent the transfer functions of the real and nominal system models, respectively. Here, the Q-filter Q_DOB is used to make G_n^{-1} physically realizable. According to Fig. 7, the disturbance estimation is given by [5]

$$\hat{d} = Q_\mathrm{DOB} \left[(\varepsilon + d) G_\mathrm{p} G_\mathrm{n}^{-1} - \varepsilon \right]. \tag{7}$$

If the system model is highly accurate ($G_\mathrm{n} \approx G_\mathrm{p}$), it can be clearly seen that $\hat{d} \approx Q_\mathrm{DOB} d$. If the Q-filter Q_DOB is a low-pass filter with a gain of 1, we have $\hat{d} \approx d$ in the low-frequency domain; therefore, we can use this disturbance estimate $\hat{d}$ to cancel the real disturbance (in the low-frequency domain), as shown in Fig. 7.

If the plant model G_n is accurate enough, the closed-loop transfer functions from d to y (plant output) in the case of PI + DOB control is given by [5, 20]

$$H_{\mathrm{PI+DOB,d}\to\mathrm{y}} \approx (1 - Q z^{-L}) H_{\mathrm{PI,d}\to\mathrm{y}}, \tag{8}$$

where z^{-L} represents the loop delay, and $H_{\mathrm{PI,d}\to\mathrm{y}}$ is the closed-loop transfer function from d to y in the case of PI control.

Because the cavity half-bandwidth ($f_{0.5} \approx 130$ Hz) is much smaller than other RF components in the plant, and the cavity detuning (during the flat-top acceleration of the RF pulse) is well compensated by the resonance control
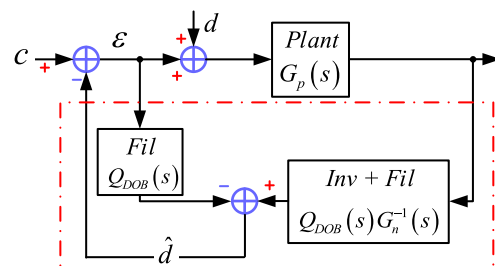
Fig. 7 (Color online) Principle of DOB control with a Q-filter

system, the transfer function of G_n can be simplified to [5, 20]

$$G_n(s) = \frac{2\pi f_{0.5}}{s + 2\pi f_{0.5}}, \tag{9}$$

where plant gain was normalized to 0 dB. The assumed restrictions of the mismatch in G_n and the uncertainties in plant G_p are listed in Table 1. The P gain was set to 100, while the I gain was set to $130 \cdot 2\pi$ to cancel the pole in the plant. These gain settings were kept the same in the case of PI and P control and PI + DOB and P + DOB control. Under these assumptions, the magnitude responses of $1 - Qz^{-L}$ and $H_{d \to y}$ are illustrated in Fig. 8. DOB control exhibits better performance in terms of disturbance rejection in the low-frequency region.

The bandwidth of Q_{DOB} restricts the effective bandwidth of DOB control. DOB control does not work if the frequency of the disturbance is larger than the bandwidth of Q_{DOB}. The determination of Q_{DOB} is a compromise among performance, robustness, and complexity.

During cERL beam commissioning, this DOB control method was demonstrated by successfully compensating the beam loading, as well as by successfully suppressing the power supply ripples and microphonics [5, 20]. It should be mentioned that the disturbances in the cERL are mainly concentrated in the low-frequency domain (less than several kilohertz).

4 Combined control approach

In our design, we incorporated the ILC algorithm and DOB control with the traditional P controller. An overall control block diagram is shown in Fig. 9.

The model $G_p(s)$ represents the transfer function of the actual plant that needs to be controlled (a combination of an RF cavity, RF sources, a preamplifier, an I/Q detector, a digital filter, etc.). In practice, this model can be acquired using a modern system identification method [10]. The model e^{-sT_d} represents the time delay in the plant. The ILC algorithms indicated by the blue block are mainly used to compensate for the repetitive errors. DOB control

Table 1 Restrictions and uncertainness in the system

Item	Value
Mismatch of plant gain	10%
Mismatch of cavity half-bandwidth	10%
Mismatch of loop delay	50%
Detuning offset	−100 Hz
Calibration error of loop phase	10°
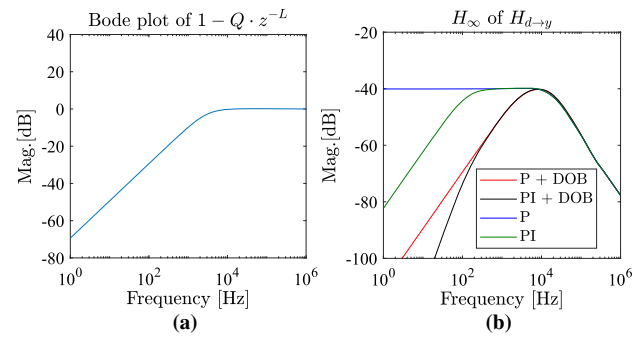
Fig. 8 (Color online) **a** Magnitude response of the block $(1 - Qz^{-L})$. **b** Upper boundary for the singular values of the closed-loop transfer function from d to y
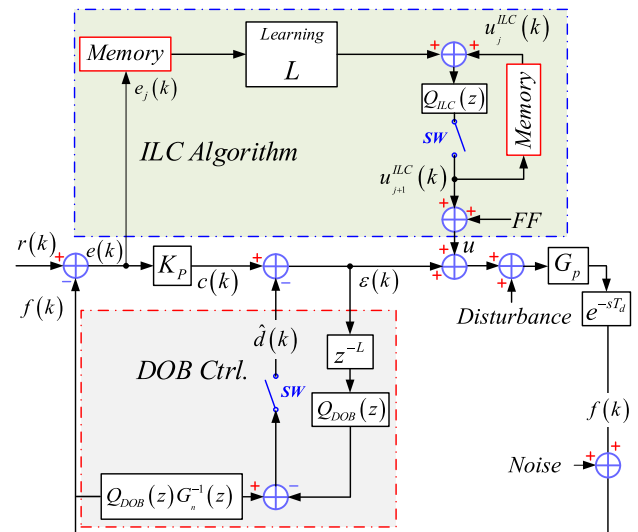
Fig. 9 (Color online) Overall model of P + DOB + ILC control. The presented ILC algorithm and DOB control are indicated by the blue and red blocks, respectively

(indicated by the red block) as well as the traditional P control are mainly used to suppress unpredictable errors. As discussed above, we adopted a plant-inversion-based ILC in our design. It should be noted that. in the combined control algorithm, the learning function L is no longer equal to G_n^{-1}. The overall system needs to be considered, and the ILC algorithm is modified as follows [13]:

$$u_{j+1}^{ILC}(k) = Q_{ILC}\left[u_j^{ILC}(k) + T_u^{-1}e_j(k)\right], \tag{10}$$

where T_u represents the closed-loop transfer function matrix from the ILC control signal u_{j+1}^{ILC} to the plant output $f(k)$. The learning function is defined as $L = T_u^{-1}$. Note that the transfer function T_u may be different in cases with and without DOB control. Accordingly, the learning function should be updated accordingly. The model $Q_{ILC}(z)$, which is the Q-filter of the ILC algorithm, is selected as a 30th-order zero-phase FIR filter. The model $Q_{DOB}(z)$

represents the Q-filter of DOB control. To find a balance between controller complexity and performance, we selected a second-order infinite impulse response (IIR) filter for Q_{DOB}. The model z^{-L} in DOB control was used to compensate for the actual time delay T_d. The FB controller is a simple P controller with a gain of K_P. DOB control and P control were implemented in the FPGA, whereas the ILC algorithm was calculated using MATLAB, and the results were sent to the FF tables (in the FPGA) via the Experimental Physics and Industrial Control System.

Finally, the stability of the combined control needs to be discussed briefly. The robust stability of DOB control was confirmed by [5, 28–30]

$$\|\Delta(z)Q_{DOB}(z)\|_\infty \le 1, \tag{11}$$

where $\Delta(z)$ describes the uncertainties in the plant. A detailed analytical study of DOB control can be found in [5, 20, 28–30]. Figure 10 shows H_∞ of P + DOB control in terms of different values of $f_{Q, DOB}$ (with a 3-dB bandwidth of Q_{DOB}). The restrictions are listed in Table 1. According to Fig. 10, we usually limit $f_{Q, DOB}$ to be <20 kHz.

A sufficient condition for the asymptotic stability of the ILC algorithm is [12, 13]

$$\|Q_{ILC}(z)[1 - L(z)T_u(z)]\|_\infty \le 1. \tag{12}$$

Setting Q_{ILC} as a low-pass filter with a gain of <1 will enhance the stability region of the ILC algorithm. Figure 11 shows plots of H_∞ of P + DOB + ILC control in terms of different values of $f_{Q, ILC}$ (with a 3-dB bandwidth of Q_{ILC}). Here, we assume that Q_{ILC} is the 30th-order zero-phase FIR filter mentioned above. $f_{Q, DOB}$ was
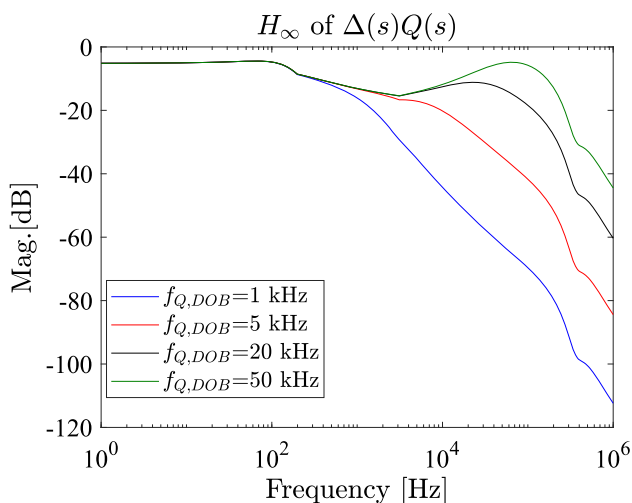
Fig. 10 (Color online) H_∞ norm of $\Delta(s)Q_{DOB}(s)$. The restrictions for the uncertainties are listed in Table 1
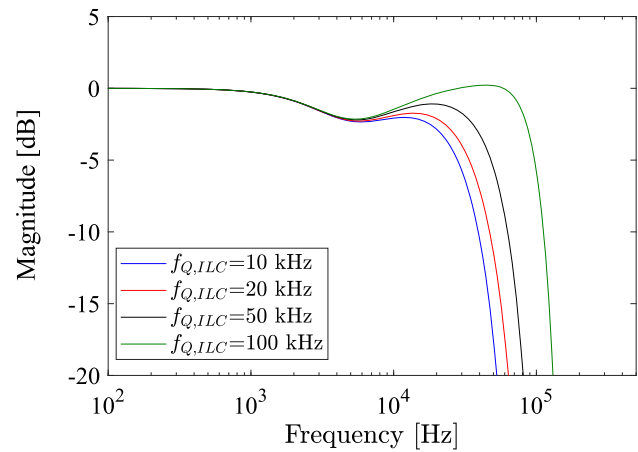
Fig. 11 (Color online) H_∞ norm of Eq. (10) determined by assuming that Q_{ILC} is the 30th-order zero-phase FIR filter

set to 3 kHz. The function L was set to $0.2T_u^{-1}$. It can be seen that the system is subjected to a risk of instability if $f_{Q, ILC} > 100$ kHz.

5 Experimental verification

P + DOB control was confirmed in the STF at KEK in the absence of the beam. The P + DOB + ILC method was demonstrated by a cavity-simulator-based test bench in which a simulated beam current was available [31, 32].

5.1 Experiment on the STF SC cavity

In the STF, cavities #1 and #2 were selected to demonstrate P + DOB control. The ILC algorithm was not included because of the absence of a beam. The loaded Q values of these two cavities were $\sim 4.6 \times 10^6$. The Q-filter Q_{DOB} in the DOB controller was a second-order IIR filter with a 5-kHz bandwidth.

Figure 12 compares the performance of the LLRF system operated with a 22.5 MV/m accelerating field ($E_{acc} \approx 22.5$ MV/m) under P control and P + DOB control. P and DOB control were activated during the filling time and flat-top time. The same loop gain (G_{loop}) of 150 and the same time-independent FF model were applied in both cases. In the case of P control, there is a tilt in the flat top of the cavity field (vector sum) for both amplitude and phase [33]. The reason for this tilt is not yet well understood. Possible sources are the LFD effect, the high-voltage power supply, and the clock distribution system. It appears that the LFD effect is not the main reason because the tilt exists even after activating the piezo tuner. In the P + DOB case, this tilt error is well compensated for by DOB control. The amplitude and phase stability of the vector-sum signal
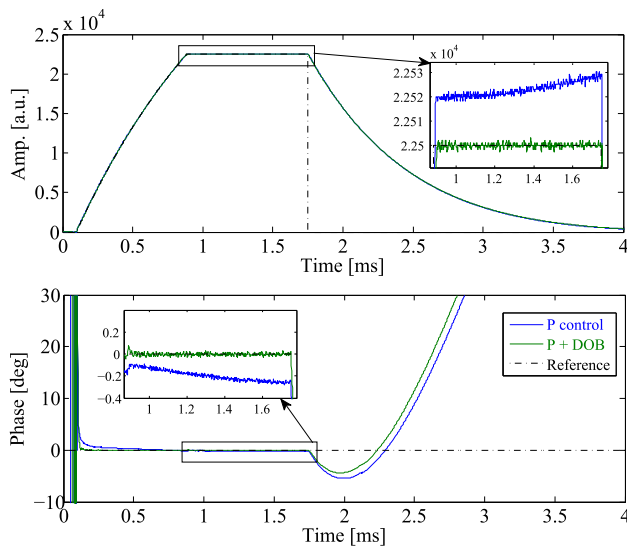
Fig. 12 (Color online) Comparison of the LLRF system under P control (in blue) and P + DOB control (in green) operated with a 22.5 MV/m field. The tilt appearing in the P control is well compensated by P + DOB control. The piezo was not activated in this experiment

(after a 250-kHz IIR filter [34]) in the flat-top profile is 0.005% (RMS) and 0.01°. (RMS), respectively. During RF commissioning, we found that the output power of the RF source was slightly increased because the noise level was enhanced by G_n^{-1} [20]. This situation can be improved by reducing $f_{Q, DOB}$; a compromise is therefore required.

Figure 13 shows the pick-up signal of cavity #1 (individual control) with a 30 MV/m accelerating field
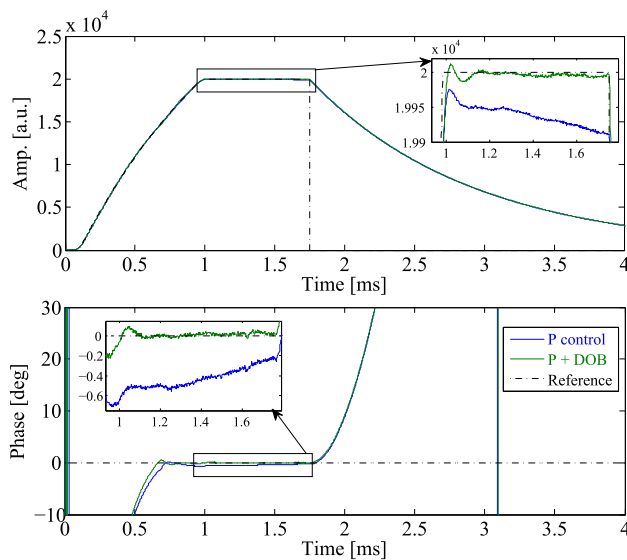
Fig. 13 (Color online) Comparison of the LLRF system under P control (in blue) and P + DOB control (in green) operated with a 30 MV/m field. The tilt appearing in the P control is well compensated by P + DOB control. The piezo is activated to compensate for the LFD effect in the flat top

($E_{acc} \approx 30$ MV/m) under P control and P + DOB control. Because of the huge LFD in the rise time, both P and DOB control start from the end of the rise time and keep activating during the entire flat-top time. Furthermore, to reduce the required klystron power during the filling time, the LFD effect was compensated for by using a method known as filling on resonance [35]. The loop gain G_{loop} was set to 100 to secure a compromise between performance and robustness. The piezo tuner was activated to compensate for the LFD effect in the flat-top region. The tilt error that appeared in P control was well compensated by P + DOB control. The stabilities of the amplitude and phase signals (after a 250-kHz IIR filter) were $\sim 0.01\%$ (RMS) and 0.02° (RMS), respectively.

It should be mentioned that we can improve system performance by adopting higher PI gains; however, higher gains lead to a deteriorated stability in the RF field because of the enhancement of the noise level of the high-frequency components [20]. In addition, higher gains also decrease the phase margin and increase the risk of an unstable loop [36]. However, DOB control will not significantly influence the characteristic polynomial (and gain margin) of the system according to the analytical study in Refs. [5, 20].

5.2 Experiment on a cavity simulator

To demonstrate the ILC algorithm in the presence of a beam, we established a cavity-simulator-based test bench [31, 32] with two FPGAs, as shown in Fig. 14. FPGA #1 was used as the cavity simulator. The main components of the simulator include the cavity baseband models for the fundamental mode (π mode) and parasitic modes ($8\pi/9$ mode), a mechanical model of the LFD, a klystron model, and models for the beam current and microphonics. The parameters of the cavity and RF system were selected mainly based on the STF facility ($Q_L \approx 4.6 \times 10^6$, 1.65-ms RF pulse, and 5-Hz repetition rate). The accelerating field was selected to be ~ 25 MV/m. FPGA #2 implemented combined control algorithms including P control, DOB control, and the ILC algorithm. For convenience, the loop gain G_{loop} and P gain K_P were adjusted to be approximately the same. It should be mentioned that the calculation of the main ILC algorithms was performed in MATLAB. The calculation result is returned to FPGA #2 using the Experimental Physics and Industrial Control System. To achieve a better transient performance, these three controllers were activated with different timelines, as shown in Fig. 15. The P gain K_P was gradually increased from 0 (at the beginning of the filling time) to 150 (at the beginning of the flat top) and remained constant in the flat-top region. DOB control was activated in the latter part of
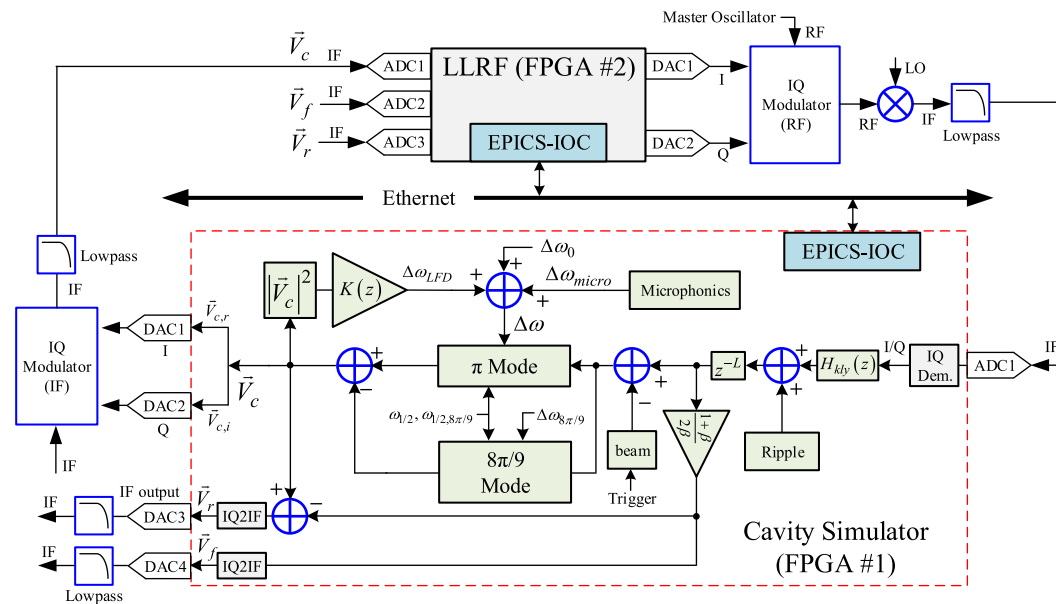
Fig. 14 (Color online) Cavity-simulator-based test bench. FPGA #1 implements the cavity simulator, while FPGA#2 realizes the presented combined algorithms
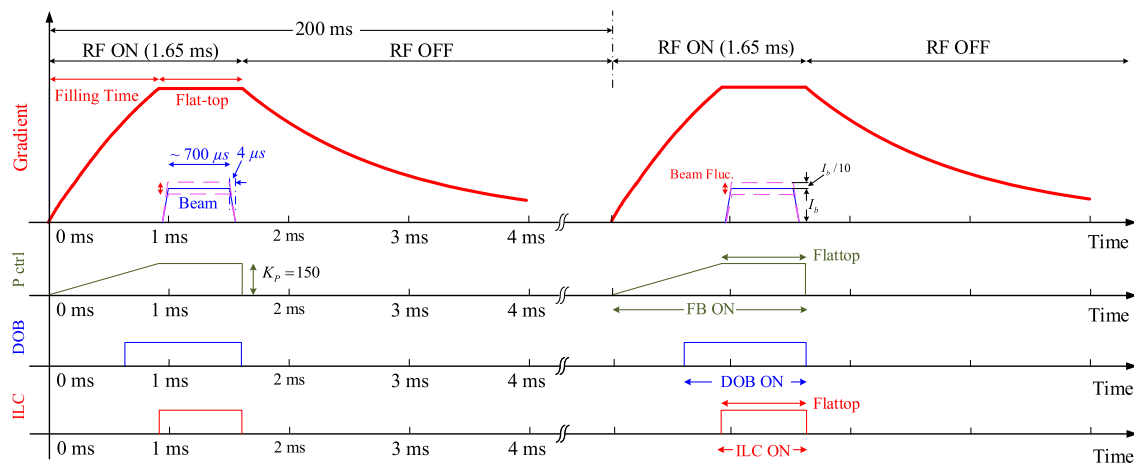
Fig. 15 (Color online) Activation time of each control method in the cavity-simulator-based test bench

the filling time, as well as during the entire flat-top time. ILC was activated only during the flat-top time.

We carefully selected the scale of the microphonics and the LFD to simulate the real STF environment. A trapezoidal 3.5-mA beam current (average beam) with a very steep edge (4 μs) was introduced into the cavity simulator. The beam width was ~ 700 μs, and it was assumed that the beam was operated nearly on-crest (i.e., beam phase ≈ 0). Furthermore, the amplitude of the beam was modulated to simulate beam fluctuation ($\Delta A / A = \pm 10\%$ peak to peak; see Fig. 15).

The plant-inversion-based ILC and a zero-phase FIR filter were adopted in our design. To obtain a better

transient response, the algorithm in Eq. (10) was modified as follows:

$$u_{j+1}^{\mathrm{ILC}}(k) = Q_{\mathrm{ILC}} \left[u_j^{\mathrm{ILC}}(k) + \alpha T_u^{-1} e_j(k + n_{\mathrm{d}}) \right], \qquad (13)$$

where the parameter α is the gain of the ILC. The selection of α is a compromise between convergence rate and performance. The term n_{d} is used to compensate for the loop delay in the system.

The iteration process of ILC control is shown in Fig. 16. The notation "j" represents the iteration index. The FF table was modified gradually for better beam compensation from pulse to pulse, and the beam-induced voltage became increasingly lower. $u_{\mathrm{I/Q}}$ and $f_{\mathrm{I/Q}}$ represent the I/Q
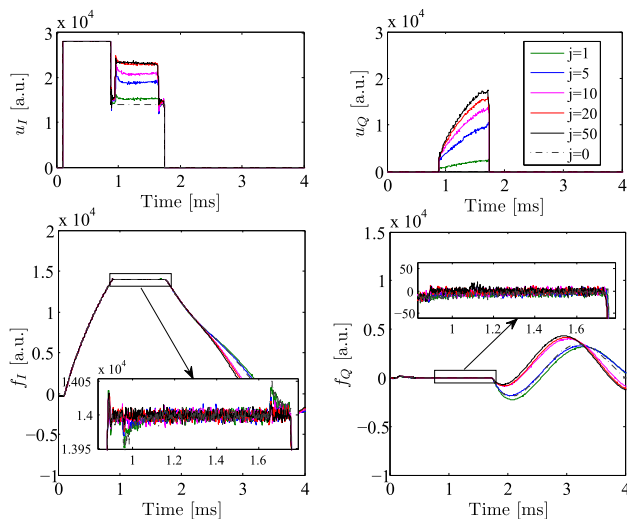
Fig. 16 (Color online) I/Q components of the plant input (u_I and u_Q) and output (f_I and f_Q) signals. The notation "j" represents the iteration index. The parameter α is 0.2

components of $u_{j+1}^{\text{ILC}}(k) + FF$ and $f(k)$, respectively (see Fig. 9).

Figure 17 compares the performance of P control, P + DOB control, P + ILC, and P + DOB + ILC. The beam conditions, disturbance level (microphonics), system gains ($G_{\text{loop}} \approx 150$), and the initial FF table were exactly same in all of these four cases. In the P control case, a very clear beam-loading effect can be observed ($\sim -0.25\%$) in the amplitude and a tilt appears in the waveform of the phase (mainly caused by the LFD effect). In the P + DOB case, the tilt is well compensated in the phase, but the beam-loading effects in the amplitude still exist in the heads and tails of the beams. The main reason for this is that the
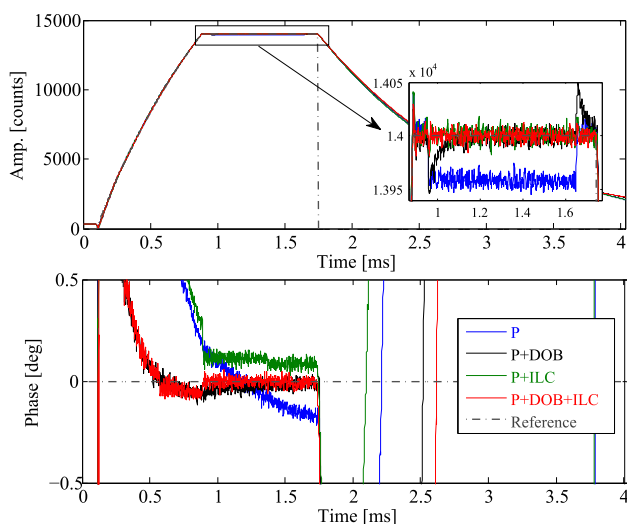
bandwidth of DOB control is limited by the Q-filter, which is ~ 3 kHz in our case. The very steep edge of the beam includes several high-frequency components, which cannot be compensated for by DOB control. In the P + ILC case, beam-loading effects are well compensated by the ILC algorithm, but a small tilt still exists in the phase, mainly because the microphonics and the 10% beam fluctuations are different from pulse to pulse. In the P + DOB + ILC control case, both the beam-loading effects and the phase tilt are perfectly compensated. It was found that application of the zero-phase filter (Q_{ILC}) improves the performance of the ILC algorithm, as shown in Fig. 18. The cavity pick-up signals in the steady state were compared with the 30th-order conventional FIR filter and zero-phase FIR filter (with 0 dB gain). A large error remains in the phase of the conventional FIR case but is almost removed by the zero-phase FIR filter.

The cutoff bandwidth of the zero-phase filter Q_{ILC} was selected based on Fig. 19. For a bandwidth of 10 kHz, the performance was poor; however, for a bandwidth as high as 120 kHz, the system could become unstable owing to the uncertainties in the model. This result is consistent with Fig. 11. According to Fig. 19, the bandwidth of Q_{ILC} was set to 70 kHz in our design.

Figure 20 compares the convergence rate for different learning functions. The blue line is the plant-inversion-based ILC with the same learning algorithm in Eq. (13), whereas the red line is the P-type ILC with the learning algorithm in Eq. (3). The parameter α was ~ 0.4 in the plant-inversion-based ILC. For a fair comparison, the proportional gain P in the P-type ILC was set to $0.4G_{\text{loop}}$. It can be clearly seen that plant-inversion-based ILC has a faster convergence rate, as expected.

Fig. 17 (Color online) Comparison of the different control methods. The parameter α is 0.2
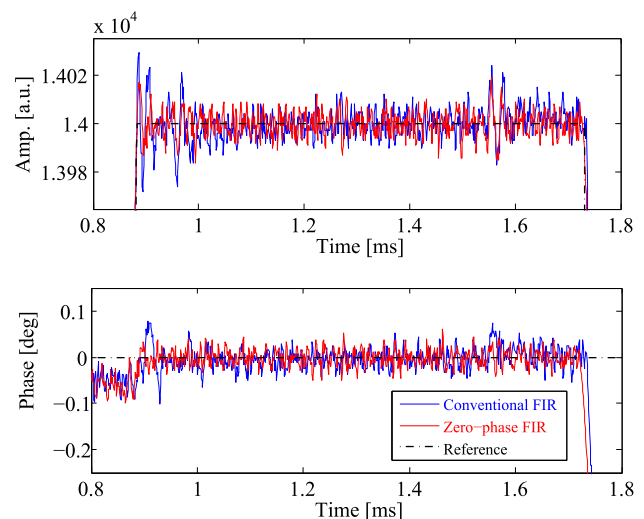
Fig. 18 (Color online) Comparison of the zero-phase FIR (in red) and conventional FIR (in blue) filters. The parameter α is 0.2 in both cases
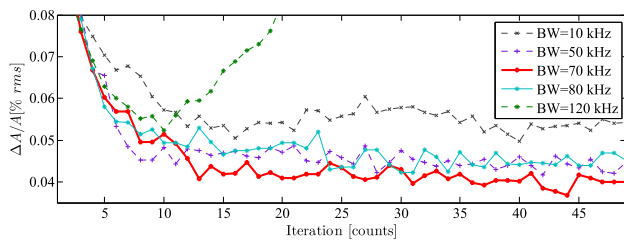
Fig. 19 (Color online) Comparison of different Q_{ILC} bandwidths. The parameter α is 0.2 in all cases
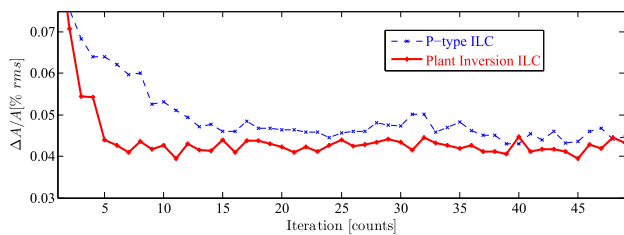
Fig. 20 (Color online) Comparison of plant-inversion-based ILC and P-ILC. The parameter α in plant-inversion-based ILC is 0.4, whereas the parameter k_{p} in P-type ILC is set to $0.4G_{\mathrm{loop}}$

6 Summary

To compensate for both the repetitive and nonrepetitive disturbances in the RF system of the International Linear Collider project, we incorporated the ILC algorithm and DOB control in the traditional P FB control system. This new P + DOB + ILC method is expected to improve the performance of the system. The PI + DOB-based control was verified in the STF in the absence of a beam. The tilt errors in the cavity field were successfully removed by using the P + DOB method. We constructed an LLRF test bench with an FPGA-based cavity simulator to demonstrate the validity of the combined P + DOB + ILC approach for beam-loading compensation. A trapezoidal beam with a steep edge was introduced into the simulator. The results demonstrated that the P + DOB + ILC method combined the advantages of both ILC and DOB and that repetitive disturbances (e.g., beam loading and LFD) and nonrepetitive disturbances (e.g., microphonics) were well compensated.

References

1. ILC, ILC Technical Design Report, available at http://www.linearcollider.org/ILC/?pid=1000895

2. H. Hayano, and STF group, Superconducting accelerator development at STF for ILC, in Proceedings of the 12th Annual Meeting of Particle Accelerator Society of Japan (PASJ2015), Tsuruga, Japan, FROL03, p. 164 (2015)

3. H. Hayano, and STF group, Progress of the STF accelerator development for ILC, in Proceedings of the 13th Annual Meeting of Particle Accelerator Society of Japan (PASJ2016), Chiba, Japan, MOOL06, p. 43 (2016)

4. Y. Yamamoto, T. Honma, E. Kako et al., High gradient cavity performance in STF-2 crymodule for ILC at KEK, in Proceedings of the seventh International Particle Accelerator Conference (IPAC'16), Busan, Korea, (JACoW, Busan, Korea, 2016), WEPMB017, p. 2158

5. F. Qiu, S. Michizono, T. Miura et al., Application of disturbance observer-based control in low-level radio frequency system in a compact energy recovery linac at KEK. Phys. Rev. ST Accel. Beams **18**, 092801 (2015). https://doi.org/10.1103/PhysRevSTAB.18.092801

6. A. Neumann. Ph.D. thesis. Humboldt-Universität zu Berlin, 2008

7. T.H. Kandil, H.K. Khalil, J. Vincent et al., Adaptive feedforward cancelation of sinusoidal disturbances in superconducting RF cavities. Nucl. Instrum. Methods Phys. Res. Sect. A. **550**, 514–520 (2005). https://doi.org/10.1016/j.nima.2005.05.060

8. M. Uchiyama, Formation of high speed motion pattern of mechanical arm by trial. Trans. Soc. Instrum. Contr. Eng. **14**, 6 (1978). https://doi.org/10.9746/sicetr1965.14.706 (**in Japanese**)

9. S. Arimoto, S. Kawamura, F. Miyazaki, Bettering operation of robots by learning. J. Robot. Syst. **1**, 123–140 (1984). https://doi.org/10.1002/rob.4620010203

10. C. Schmidt, Ph.D. thesis, Technische Universität Hamburg-Harburg (2010)

11. S. Kichhoff, C. Schmidt, G. Lichtenberg et al., An iterative learning algorithm for control of an accelerator based free electron laser, in Proceedings of the 47th IEEE Conference on Decision and Control Cancun, Mexico, (IEEE, Cancun, Mexico, 2008), p. 3032. https://doi.org/10.1109/CDC.2008.4739064

12. D.A. Bristow, M. Tharayil, A.G. Alleyne, A survey of iterative learning control. IEEE Control Syst. **26**, 96–114 (2006). https://doi.org/10.1109/MCS.2006.1636313

13. Shu-Wen Yu, Ph.D. thesis, University of California, Berkeley (2011)

14. M. Laverty, K. Fong, An Iterative Learning Feedforward Controller for the TRIMUF E-LINAC, in Proceedings of 28th Linear Accelerator Conference (LINAC'16), East Lansing, MI, USA, (JACoW, East Lansing, MI, USA), TUPLR009, p. 485

15. K. Ohishi, M. Nakao, K. Ohnishi et al., Microprocessor-controlled DC motor for load-insensitive position servo system. IEEE Trans. Ind. Electron. **IE34**, 44–49 (1987). https://doi.org/10.1109/TIE.1987.350923

16. T. Umeno, Y. Hori, Robust speed control of DC servomotors using modern two-degree-of-freedom controller design. IEEE Trans. Ind. Electron. **38**, 5 (1991). https://doi.org/10.1109/41.97556

17. F. Qiu, D. Arakawa, Y. Honda et al., A disturbance-observer-based controller for LLRF systems, in Proceedings of the sixth International Particle Accelerator Conference (IPAC'15), Richmond, USA, (JACoW, Richmond, USA, 2015), WEPMA054, p. 2895. https://doi.org/10.18429/JACoW-IPAC2015-WEPMA054

18. S. Sakanaka, M. Adachi, S. Adachi et al., Construction and commissioning of compact erl injector at KEK, in Proceedings of the 53rd ICFA Advanced Beam Dynamics Workshop on Energy Recovery Linac (ERL2013) (Russia, Novosibirsk, 2013)

19. N. Nakamura, M. Adachi, S. Adachi et al., Present status of compact ERL at KEK, in Proceedings of the 5th International

Particle Accelerator Conference (IPAC'14), Dresden, Germany, (JACoW, Dresden, Germany, 2014) MOPRO110, p. 353

20. F. Qiu, T. Miura, D. Arakawa et al., Application of disturbance observer-based control on pulsed superconducting radio frequency cavities. Phys. Rev. Accel. Beams **24**, 012804 (2021). https://doi.org/10.1103/PhysRevAccelBeams.24.012804

21. T. Schilcher, Ph.D. Thesis, Universität Hamburg (1998)

22. Z.Q. Geng, Beam based optimization of SwissFEL low-level RF system. Nucl. Sci. Tech. **29**, 128 (2018). https://doi.org/10.1007/s41365-018-0460-7

23. Z.Q. Geng, R. Kalt, Advanced topics on RF amplitude and phase detection for low-level RF systems. Nucl. Sci. Tech. **30**, 146 (2019). https://doi.org/10.1007/s41365-019-0670-7

24. T. Matsumoto, S. Fukuda, H. Katagiri et al., Digital low-level RF control system with four intermediate frequencies at STF, in Proceedings of the 23rd Particle Accelerator Conference, Vancouver, Canada, 2009, (JACoW, Vancouver, Canada, 2009), WE5PFP086

25. Z.Q. Geng, Superconducting cavity control and model identification based on active disturbance rejection control. IEEE Trans. Nucl. Sci. **64**, 951–958 (2017). https://doi.org/10.1103/PhysRevSTAB.18.0928010

26. H. Elci, R.W. Longman, M.Q. Phan et al., Simple learning control made practical by zero-phase filtering: applications to robotics. IEEE Trans. Circuits Syst. I Fundam. Theory Appl. **49**, 753–767 (2002). https://doi.org/10.1103/PhysRevSTAB.18.0928011

27. MathWorks, https://www.mathworks.com/help/signal/ug/anti-causal-zero-phase-filter-implementation.html

28. C.J. Kempf, S. Kobayashi, Discrete-time disturbance observer design for systems with time delay, in Proceedings of Advanced Motion Control, 1996 4th International Workshop (AMC'96-MIE), Mie, Japan, (**1**), (IEEE, Mie, Japan, 1996). https://doi.org/10.1109/AMC.1996.509428

29. X. Chen, M. Tomizuka, Optimal plant shaping for high bandwidth disturbance rejection in discrete disturbance observers in Proceedings of American Control Conference (ACC), Baltimore, MD, USA (IEEE, Baltimore, MD, USA, 2010), p. 2641. https://doi.org/10.1109/ACC.2010.5531256

30. W. Li, Y. Hori, Vibration suppression using single neuron-based PI fuzzy controller and fractional-order disturbance observer. IEEE Trans. Ind. Electron. **54**, 117–126 (2007). https://doi.org/10.1103/PhysRevSTAB.18.0928012

31. T. Czarski, K.T. Pozniak, R.S. Romaniuk et al., TESLA cavity modeling and digital implementation in FPGA technology for control system development. Nucl. Instr. Methods A **556**, 565–576 (2006). https://doi.org/10.1103/PhysRevSTAB.18.0928013

32. F. Qiu, S. Michizono, T. Miura et al., Real-time cavity simulator-based low-level radio frequency test bench and applications for accelerators Phys. Rev. Accel. Beams **21**, 032003 (2018). https://doi.org/10.1103/PhysRevSTAB.18.0928014

33. S.B. Wibowo, T. Matsumoto, S. Michizono et al., IF mixture performance during cavity conditioning at STF-KEK. in Proceedings of 28th Linear Accelerator Conference (LINAC'16), East Lansing, MI, USA, (JACoW, East Lansing, MI, USA), TUPLR009, p. 485

34. F. Qiu, S. Michizono, T. Miura et al., Digital filters used for digital feedback system at cERL, in Proceedings of the 27th Linear Accelerator Conference, LINAC14, Geneva, Switzerland, 2014 (JACoW, Geneva, Switzerland, 2014), MOPP074, p. 227

35. V. Ayvazyan, S. Choroba, Z.Q. Geng et al., Optimization of Filling Procedure for TESLA-type Cavities for Klystron RF Power Minimization for European XFEL, in Proceedings of International Particle Accelerator Conference (IPAC'10), Kyoto, Japan, (JACoW, Kyoto, Japan, 2016), TUPEA039, p. 1416

36. K. Umemori, M. Egi, K. Enami et al., Long-term operation experience with beams in compact ERL crymodules, in Proceedings of the 18th International Conference on RF Superconductivity, SRF2017, Lanzhou, China, 2017 (JACoW, Geneva, 2017), THYA06, p. 736. https://doi.org/10.18429/JACoW-SRF2017-THYA06